

Showcasing research from Professor Hyun You Kim's laboratory, Department of Materials Science and Engineering, Chungnam National University, Daejeon, Korea

A tailored oxide interface creates dense Pt single-atom catalysts with high catalytic activity

Dense Pt-single atoms (SAs) homogeneously distributed over the surface of oxide supports guarantee the optimum materials' efficiency by using all individual Pt atoms as reaction sites. However, even for simple CO oxidation reaction, achieving the high catalytic performance of Pt-SAs is challenging because Pt-SAs are structurally vulnerable and Pt-SAs are easily CO-poisonable. Herein, we report on highly reactive and CO-tolerant dense Pt-SAs formed at the $\text{CeO}_x\text{-TiO}_2$ interfaces. Our atomic-scale interface tuning strategy provides a promising approach toward rational design of SA catalysts with excellent catalytic performance and high materials' efficiency.

As featured in:



See WooChul Jung, Chunjoong Kim, Hyun You Kim *et al.*, *Energy Environ. Sci.*, 2020, **13**, 1231.

Cite this: *Energy Environ. Sci.*, 2020, 13, 1231

A tailored oxide interface creates dense Pt single-atom catalysts with high catalytic activity†

Mi Yoo,^{‡a} Young-Sang Yu,^{‡b} Hyunwoo Ha,^{id ‡a} Siwon Lee,^{‡c} Jin-Seok Choi,^d Sunyoung Oh,^{ef} Eunji Kang,^a Hyuk Choi,^a Hyesung An,^{id a} Kug-Seung Lee,^{id g} Jeong Young Park,^{id ef} Richard Celestre,^b Matthew A. Marcus,^b Kasra Nowrouzi,^b Doug Taube,^b David A. Shapiro,^b WooChul Jung,^{id *c} Chunjoong Kim^{*a} and Hyun You Kim^{id *a}

Highly reactive dense Pt single-atoms stabilized on an oxide support can resolve a grand challenge in the economic use of Pt in catalysis. The maximized number density of reaction sites provided by dense Pt single-atoms guarantees the improved catalytic performance of Pt combined with high efficiency. By manipulating the chemical nature of multi-component interfaces, we synthesized CO-tolerant dense Pt single-atoms highly reactive for the CO oxidation reaction, which governs the key steps for chemical energy conversion and emission control. The addition of 1 wt% of Ce to TiO₂ support particles creates a CeO_x-TiO₂ interface that stabilizes Pt single-atoms by strong electronic interactions. Dense Pt single-atoms formed on CeO_x/TiO₂ oxides exhibit 15.1 times greater specific mass activity toward CO oxidation at 140 °C compared with a bare Pt/TiO₂ catalyst. We elaborate how the CeO_x-TiO₂ interfaces activate the interface-mediated Mars-van Krevelen mechanism of CO oxidation and protect Pt single-atoms from CO-poisoning. Through a comprehensive interpretation of the formation and activation of dense Pt single-atoms using *operando* X-ray absorption spectroscopy, density functional theory calculations, and experimental catalyst performance tests, we provide a key that enables the catalytic performance of noble metal single-atom catalysts to be optimized by atomic-scale tuning of the metal-support interface.

Received 29th October 2019,
Accepted 18th December 2019

DOI: 10.1039/c9ee03492g

rsc.li/ees

Broader context

Oxide supported Pt nanoparticle (NP)-based catalysts accelerate many critical chemical reactions for energy conversion and emission control. Achieving high catalytic performance of Pt catalysts, while using less Pt, is key for sustainable use of earth un abundant Pt. The relevant catalysis communities are responding to such needs by reducing the size of Pt NPs to sub-nanometer or even pulverizing Pt NPs into single-atoms (SAs). Dense Pt-SAs homogeneously distributed over the surface of oxide supports guarantee the optimum material efficiency by using all individual Pt atoms as reaction sites. However, even for the simple CO oxidation reaction, achieving high catalytic performance of Pt-SAs is challenging because Pt-SAs are structurally vulnerable and easily CO-poisonable. In this study, we accomplished the catalytic supremacy of Pt-SAs using a CeO_x/TiO₂ hybrid-oxide support and manipulating the chemical nature of multi-component interfaces. The highly reactive and CO-tolerant dense Pt-SAs formed at the CeO_x-TiO₂ interfaces exhibit outstanding catalytic performance toward CO oxidation compared with conventional Pt NP-based catalysts. Our atomic-scale interface tuning strategy provides a promising approach toward rational design of SA catalysts with excellent catalytic performance and high material efficiency.

^a Department of Materials Science and Engineering, Chungnam National University, Daejeon 34134, Republic of Korea. E-mail: ckim0218@cnu.ac.kr, kimhy@cnu.ac.kr^b Advanced Light Source, Lawrence Berkeley National Laboratory, Berkeley, California 94720, USA^c Department of Materials Science and Engineering, Korea Advanced Institute of Science and Technology (KAIST), Daejeon 34141, Republic of Korea. E-mail: wcjung@kaist.ac.kr^d KAIST Analysis Center for Research Advancement, Korea Advanced Institute of Science and Technology (KAIST), Daejeon 34141, Republic of Korea^e Center for Nanomaterials and Chemical Reactions, Institute for Basic Science (IBS), Daejeon 34141, Republic of Korea^f Department of Chemistry, Korea Advanced Institute of Science and Technology (KAIST), Daejeon 34141, Republic of Korea^g Pohang Accelerator Laboratory, Pohang University of Science and Technology, Pohang 37673, Republic of Korea

† Electronic supplementary information (ESI) available: Detailed experimental and theoretical methods and additional characterization. See DOI: 10.1039/c9ee03492g

‡ These authors contributed equally to this work.

Introduction

The cutting edge of rational design of heterogeneous catalysts drives the efficient use of expensive noble metals. Intriguing studies on the catalytic properties of isolated metal ions embedded within oxide supports^{1,2} or sub-nanometer-sized cluster catalysts^{3–5} have provided innovative ideas on the use of low-dimensional motifs of noble metals for enhancing the catalytic activity. Recent studies have explored the catalytic functionality of single-atom (SA) catalysts.^{6–12} The greater surface area of SAs spontaneously increases the number density of reaction sites, which in turn enhances the specific mass activity (MA) of the catalyst.^{8,11–13} Moreover, given the improved chemical and physical homogeneity of the reaction sites, SA catalysts often comprise outstanding selectivity along with enhanced activity.^{14,15}

Although the design of SA-based heterogeneous catalysts is newly emerging, several fundamental issues have not yet been resolved.¹⁶ Achieving high catalytic activity¹⁶ in SA catalysts requires the design of catalysts with well-distributed, dense metal monomers. Recent efforts toward stabilization of SAs showed that the chemical potential of SAs can be tuned by utilizing the SA-support^{17–19} and SA-reactant interactions.^{10,18–20} Particularly, CeO₂ and TiO₂ are known as the best supporting oxides for stabilization of Pt-SAs.^{16,21} The strong interaction between Pt-SAs and supporting oxides leads to preferred formation of ionic Pt species.²¹ However, synthesis of dense SAs on such supports for further improved conversion performance is still challenging.¹⁶

In addition to the structural issues, it is still unclear whether the inherent catalytic nature of SAs is different from the nanoparticle (NP) counterparts and if SAs are superior to NPs for a given reaction. The interfaces between Pt NPs and oxide supporting materials are generally regarded as a reaction site for oxidation.^{22–24} Naturally, as Pt NPs are pulverized into Pt-SAs, the total length of the Pt-oxide interface increases. However, whether the interface between a Pt-SA and an oxide support exhibits the same catalytic activity as the interface between a Pt NP and an oxide is unknown. Even in the case of CO oxidation, the catalytic behaviour of Pt-SAs is controversial.^{25,26} Stair and coworkers identified Pt NPs rather than Pt-SAs as the more efficient catalyst for CO oxidation since Pt-SAs are readily deactivated by CO-poisoning.²⁵ Meanwhile, Pt-SAs supported on 5 nm-sized TiO₂ NPs are reported to reveal the Mars-van Krevelen (MvK) type of CO oxidation ($\text{CO}_{\text{ad}} + \text{O}_{\text{lattice}} \rightarrow \text{CO}_2(\text{g})$) and are inherently immune to CO-poisoning.²⁷ Moreover, Nie *et al.* demonstrated that the CO oxidation activity of Pt-SAs supported on CeO₂ NPs can be improved by steam treatment, corroborating the importance of the chemical nature of the oxygen species at the Pt-CeO₂ interface for activation of the MvK type CO oxidation by Pt-SAs.⁷ These results suggest that the catalytic reaction mechanism of oxide supported SAs is strongly correlated with the chemical nature of the metal-oxide interfaces, whose areal fraction is maximized in SA-based catalysts. Designing an appropriate supporting material is essential to achieve ideal performance of SA-based catalysts.

CO oxidation has been applied as a prototypical reaction for catalysis studies due to its relatively simple chemistry.²⁸ The US Department of Energy 150 °C challenge for emissions (converting 90% of pollutants in automotive exhaust gas at 150 °C)²⁹ is driving the design of highly reactive and efficient CO oxidation catalysts for environmental applications.¹⁶ Moreover, CO oxidation is a key step for chemical energy conversion such as the water-gas shift reaction.^{30,31}

Pt catalysts are prone to CO-poisoning, therefore removal of CO from the hydrogen feedstock (below 10 ppm^{32,33}) is critical when Pt catalysts are applied in polymer electrolyte fuel cells (PEMFCs).^{32,33} In this aspect, hydrogen purification through preferential oxidation (PROX) of CO under high H₂ partial pressure conditions^{33–37} is becoming more important. A highly CO-tolerant Pt catalyst would guarantee the improved reliability of fuel cell-based energy generating systems. Moreover, a Pt-based catalyst with both CO-immunity and high catalytic activity can significantly increase the reliability and efficiency of the catalytic reaction activated by Pt under CO-rich conditions.

In parallel, the formation of ionic Pt-SAs on oxide supports is accompanied by the oxidation state change of the supporting oxide, especially at the interface region.³⁸ Thus, observing the oxidation state of the supporting oxide plays a crucial role in uncovering the mechanism of CO oxidation. For example, reduction of Ce ions at the Pt-CeO₂ interface during CO oxidation accounts for the operation of the MvK type CO oxidation by Pt-SAs. Recently, site-specific infrared (IR) spectroscopy²⁵ and near-ambient pressure X-ray photoelectron spectroscopy³⁸ provided insights for identifying the catalytic active sites but these methods lack spatial information. Additionally, a combination of extended X-ray absorption fine structure (EXAFS) and environmental transmission electron microscopy traced the *in situ* structural rearrangement of Pt NPs,³⁹ however, quantitative chemical information remains elusive. Thus, qualifying the spatio-temporal evolution of the oxidation state of supporting materials can elucidate both the preferred sites of Pt-SA formation during synthesis and the underlying catalytic mechanism. Particularly, such observations under real synthesis/working conditions in a liquid/gas have not been achieved owing to a lack of spatio-temporal resolution and information about beam-induced damage.⁴⁰

Here, we demonstrate a high-performance dense Pt-SA catalyst by designing the chemical nature of the multi-component interface with atomic precision. A CeO_x-TiO₂ hybrid-oxide support was synthesized to provide strong binding sites and reactive oxygen species for Pt-SAs and, therefore, activate the interface-mediated MvK CO oxidation mechanism. We adopt synchrotron-based *operando* liquid/gas scanning transmission X-ray microscopy (STXM) to probe the spatio-temporal evolution of the Ce oxidation state, by which the preferred growth of Pt-SAs at the CeO_x-TiO₂ interfaces and the interface-mediated reaction mechanism can be elucidated.

Results and discussion

CeO₂ and TiO₂ are the most widely applied supporting oxide materials which can exceptionally stabilize Pt-SAs by formation

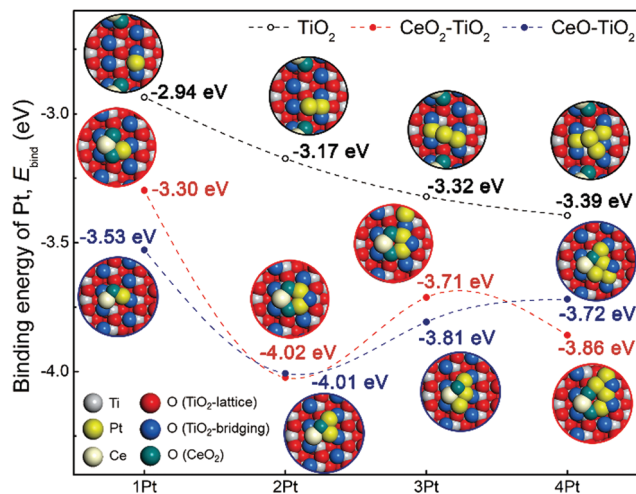


Fig. 1 DFT-calculated binding trend of Pt-SAs on TiO₂(101) and at the CeO_x-TiO₂ interface with fully oxidized or reduced Ce ions. E_{bind} of $n\text{Pt}$ represents the average binding energy of the total number of Pt atoms.

of Pt ionic species.¹⁶ We designed our Pt/CeO_x-TiO₂ (PCT) catalyst system with reference to theoretical modelling: we constructed a CeO_x-TiO₂ interface model with a single CeO₂ cluster on the (101) surface of anatase-phase TiO₂ (Fig. 1). The formation of ceria clusters on the TiO₂(101) surface is thermodynamically preferred under low Ce-loading conditions.^{41,42} Density functional theory (DFT)-calculated energies of Pt deposition on TiO₂ and at the CeO_x-TiO₂ interface confirmed that the affinity of the CeO_x-TiO₂ interface toward Pt stabilizes the Pt₂ cluster at the interface (Fig. 1). Upon deposition, Pt donates electrons to the Ce and O ions at the CeO_x-TiO₂ interface (Fig. S1 in the ESI†). Based on these promising theoretical findings, CeO_x-TiO₂ hybrid-oxides were prepared by the chemical synthesis of CeO_x nanoarchitectures on the surface of ~25 nm-sized TiO₂ particles *via* thermal reduction of cerium nitrate (Ce(NO₃)₃·6H₂O).^{42,43} Small CeO_x clusters were predominantly observed in the CeO_x-TiO₂ samples with 1 wt% of Ce addition (Fig. 2a and b), which assures the maximum concentration of CeO_x-TiO₂ interfaces and closely resembles our model structure: a single CeO₂ cluster on TiO₂(101) that can stabilize Pt-SAs by electron donation from Pt. While the Ce-loading in the CeO_x-TiO₂ hybrid-oxide was kept at 1 wt%, various amounts of Pt were impregnated on the CeO_x-TiO₂ support (hereafter, $n\text{PCT}$, where $n = 0.25, 0.5,$ and 1.0 wt%; see Table S1 in the ESI† for the composition analysis result). Corresponding control group samples, Pt catalysts on the TiO₂ support without any Ce addition ($n\text{PT}$, where $n = 0.25, 0.5,$ and 1.0 wt%), were also synthesized.

Scanning transmission electron microscopy (STEM) images of the supporting CeO_x-TiO₂ (1CT) and $n\text{PCT}$ catalysts are presented in Fig. 2. The STEM images of $n\text{PCT}$ show that tiny, bright, and highly distinguishable Pt-SAs are distributed over the surface of the $n\text{PCT}$ catalysts (Fig. 2c, e and g). Energy-dispersive X-ray spectroscopy scan images (Fig. 2d, f and h) and the intensity profiles of the selected highlighted areas of 0.5PCT (Fig. 2i and j) corroborate that the Pt-SAs are strongly

correlated with the preformed CeO_x clusters on TiO₂, thus affirming the strong Pt affinity of the CeO_x clusters. Consistent with recent findings,^{10,17,44} Pt-SAs could be preferentially synthesized owing to the SA-support interaction. On the other hand, the population of the sub-nanometer-sized Pt NPs was relatively greater in the $n\text{PT}$ samples than the $n\text{PCT}$ samples (Fig. S2 and S3 in the ESI†).

Spatio-temporal observation was performed using *operando* synchrotron-based STXM combined with a liquid flow nano-reactor (see Methods and Fig. S4 in the ESI†) to probe the preferred *in situ* Pt-SA formation onto CeO_x-TiO₂. In this case, a CeO_x-TiO₂ sample with 6 wt%, instead of 1 wt%, was used to obtain distinct absorption features (both Ce³⁺ and Ce⁴⁺, Fig. S5 and S7 in the ESI†) and measurable absorption contrast. Using a microfluidic heating cell, we tracked the change in the Ce oxidation state that accompanies the Pt-SAs growing onto CeO_x-TiO₂ (see Supplementary discussion, Fig. 3b and Fig. S6, S7 in the ESI†). Fig. 3b shows *operando* image spectra of a typical particle aggregate, which contains a statistically significant number of ~25 nm-sized CeO_x-TiO₂ particles. Although the spatial resolution of the STXM image spectra (~55 nm with a 45 nm outer-zone-width Fresnel zone plate) cannot directly visualize the individual CeO_x-TiO₂ particles or Pt-SAs, the heterogeneous distributions of the Ce oxidation states were clearly observed by analyzing X-ray absorption near-edge structure (XANES) on a pixel-by-pixel basis with reference spectra (Fig. 3b). Of particular note is that the maximum dose for an individual pixel was carefully limited to eliminate partial photoreduction of CeO₂ (see Methods and Fig. S6 in the ESI†), therefore highly reliable quantitative analysis about the Ce oxidation state was available. During the initial stage of the Pt-SA formation, the Ce oxidation states averaged over each particle were continuously reduced (Fig. 3c and d). The interactions between the Pt-SAs and CeO_x-TiO₂ induced electron transfer from Pt to Ce.

A surprising observation for the heterogeneous Ce oxidation states during the Pt-SA formation indicates a strong correlation between the initial Ce³⁺ concentration and the relative Ce oxidation state change, ΔCe^{4+} (pixel-by-pixel Ce⁴⁺ concentration differences between the first and the second image spectra, Fig. 3e). In general, the pixels in which the initial Ce³⁺ fraction is higher were more reduced during the Pt-SA formation. Since the Ce³⁺ phase is highly localized at the CeO_x-TiO₂ interface (see Supplementary discussion in the ESI†), the strong spatial correlation in Fig. 3e suggests that the CeO_x-TiO₂ interface and not the CeO₂ surface is the preferred site for Pt-SA growth. Therefore, along with our DFT calculation results and STEM observations, the *operando* STXM observations confirm the effectiveness of the CeO_x-TiO₂ interface in disintegrating Pt NPs. Interestingly, the concentration of the reduced Ce³⁺ upon Pt-SA formation recovers to the original value after further Pt deposition (after 250 min, Fig. 3d), upon emergence of Pt NPs that do not excessively donate electrons to Ce ions.

The XANES and EXAFS across the Pt L-edge also indicate that CeO_x-TiO₂ stabilizes part of the Pt-SAs even under high Pt-loading conditions ($n = 1$, Fig. S8 in the ESI†) by forming

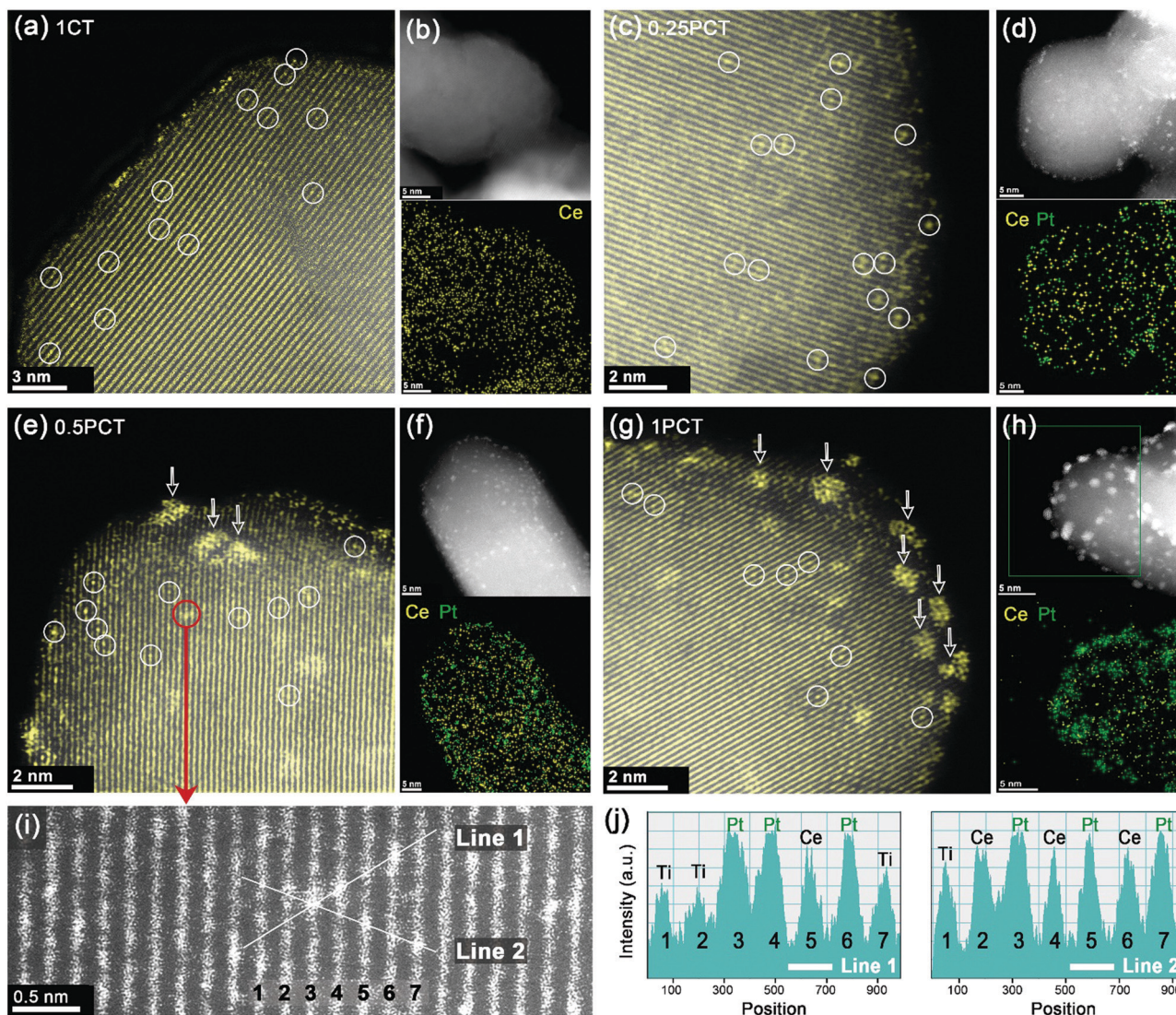


Fig. 2 Morphology of the $\text{CeO}_x\text{-TiO}_2$ support and $n\text{PCT}$ catalysts ($n \leq 1$). (a) High-angle annular dark-field (HAADF)-STEM images of the $\text{CeO}_x\text{-TiO}_2$ supporting oxide with 1 wt% initial Ce-loading. (b) HAADF-STEM and Ce EDS scan images of the $\text{CeO}_x\text{-TiO}_2$ presented in (a). HAADF-STEM image and Ce and Pt EDS scan image of 0.25PCT [(c and d)], 0.5PCT [(e and f)], and 1PCT [(g and h)]. The atomic-sized bright spots in (c, e and g) denote Pt-SAs and CeO_x clusters. Some of the CeO_x clusters and Pt-SAs are highlighted in white circles. Ce and Pt EDS scan images [(d, f and h)] confirm the locational correlation of CeO_x and Pt-SAs on TiO_2 powder surfaces. (i and j) Intensity profile of the selected highlighted area of 0.5PCT, which clearly shows the intimate contact between Pt, Ce, and Ti ions. The arrows in (e and g) indicate Pt NPs formed under the higher Pt-loading.

ionic Pt phases. This is shown by the rightward shift of the peak in the XANES, indicating an increased oxidation state for Pt, and the appearance of a peak in the EXAFS Fourier magnitude at the same position (1.7 \AA indicated) as in PtO_2 . Because the XANES spectra show that the Pt in the $n\text{PCT}$ and $n\text{PT}$ catalysts with lower n is the more ionic (PtO_2 like, Fig. S9 in the ESI[†]), all the XANES spectra were fit by a linear combination using reference standard spectra of Pt and PtO_2 to provide quantitative information (Fig. S9 and Table S2 in the ESI[†]). The relative amounts of Pt and PtO_2 in the $n\text{PT}$ and $n\text{PCT}$ catalysts also confirm the increased content of ionic Pt in $n\text{PCT}$, compared to $n\text{PT}$.

Based on our findings of the preferential formation of Pt-SAs at the $\text{CeO}_x\text{-TiO}_2$ interface, DFT calculations were geared towards

scrutinizing the mechanism of CO oxidation that could be catalyzed by Pt-SAs at the $\text{CeO}_x\text{-TiO}_2$ interface. Fig. 4 suggests the CO oxidation pathway by the $\text{Pt}_2/\text{CeO}_x\text{-TiO}_2$ model catalyst. We found that a Pt_2 cluster at the $\text{CeO}_x\text{-TiO}_2$ interface binds two CO molecules together (stages 1 and 2, hereafter S1 and S2, respectively). The interfacial oxygen ion bridging the Ce and the Ti ions and binding the Pt_2 cluster oxidizes a Pt-bound CO molecule (Pt-CO^*) through the interface-mediated MvK mechanism. The formation of an O-C-O-type intermediate requires an activation energy barrier, E_{act} , of 0.75 eV (marked as TS1, Fig. 4). After the relatively easy production of CO_2 (S3), the Ce ion of $\text{Pt}_2/\text{CeO}_x\text{-TiO}_2$ binds and activates an oxygen molecule (S4). One oxygen atom of the Ce-bound O_2 molecule oxidizes another Pt-CO^* and the other O atom heals the

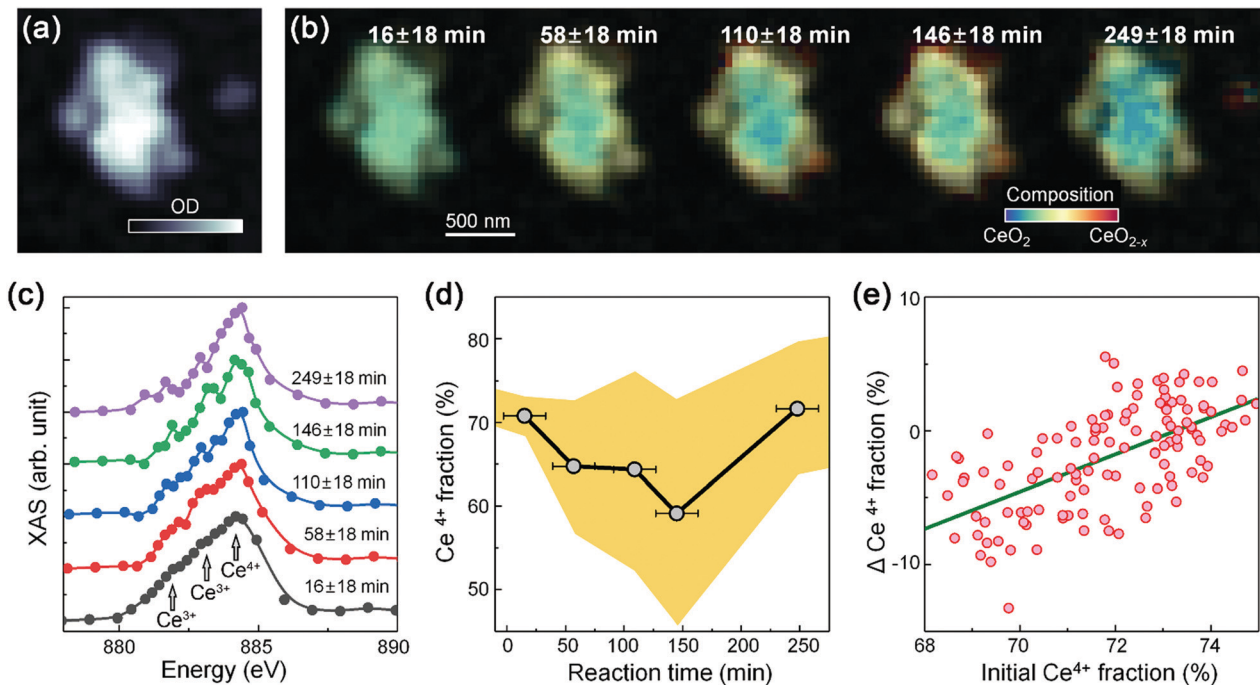


Fig. 3 Electronic interaction between Pt and Ce upon formation of Pt-SAs at the $\text{CeO}_x\text{-TiO}_2$ interfaces, which is directly observed by *operando* X-ray absorption spectroscopy. (a) Averaged optical density map across the Ce M_5 -edge. (b) Spatio-temporal chemical evolution with respect to reaction time. Chemical phase maps obtained by linear combination fits of XAS data at each pixel (see Methods in the ESI†). The fitting results (chemical information) and averaged optical density (morphological information) are shown by the color legend and transparency, respectively. The presence of CeO_2 and CeO_{2-x} was assigned to blue and red colors, respectively. (c) *Operando* XAS from the entire particle region in (a). The energy positions of the M_5 -edge absorption features for Ce^{3+} and Ce^{4+} are indicated as black arrows. (d) Ce^{4+} fraction versus reaction time. The scatter points and the yellow shaded area indicate the average and standard deviation of the Ce^{4+} fraction from the entire particle region, respectively. The error range of the reaction time is estimated by the liquid injection time (see Methods in the ESI†). (e) Distribution plot of the initial Ce^{4+} fraction versus fraction difference between the first and second measurements (solid red scatter points). The solid green line is a guide for the eye.

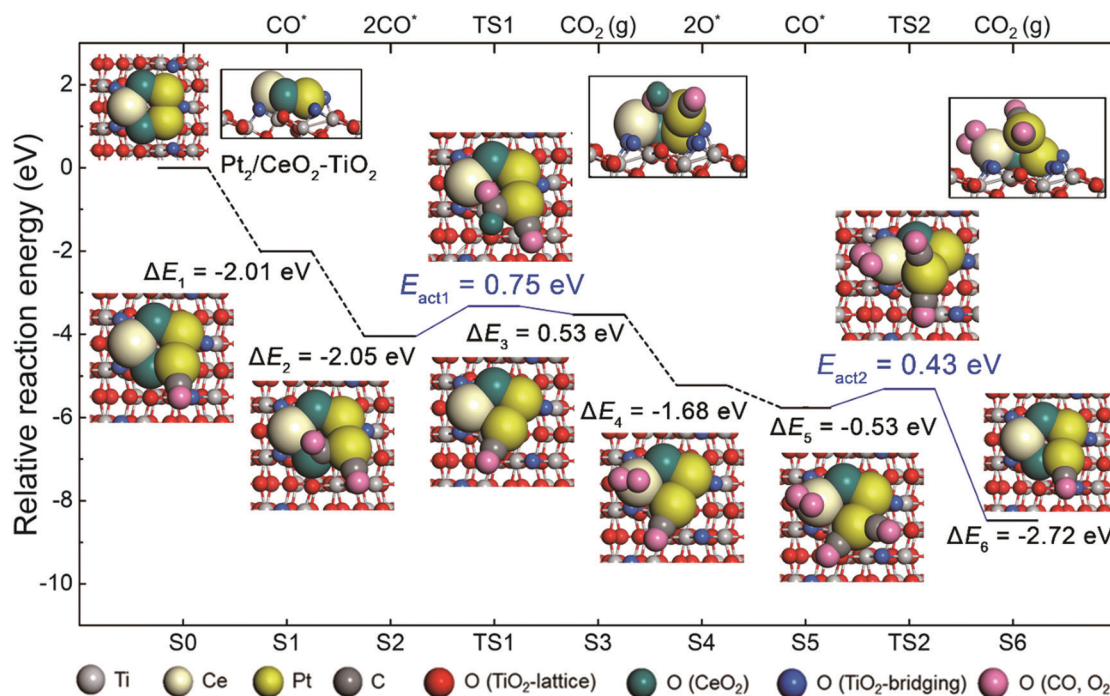


Fig. 4 DFT-predicted MvK-type CO oxidation pathway catalyzed by a Pt_2 cluster pinned at the $\text{CeO}_x\text{-TiO}_2$ interface. ΔE_n denotes the relative energy of the n^{th} stage with respect to the $(n-1)^{\text{th}}$ stage. For example, ΔE_3 was calculated as follows: $\Delta E_3 = \text{energy of stage 3} - \text{energy of stage 2}$.

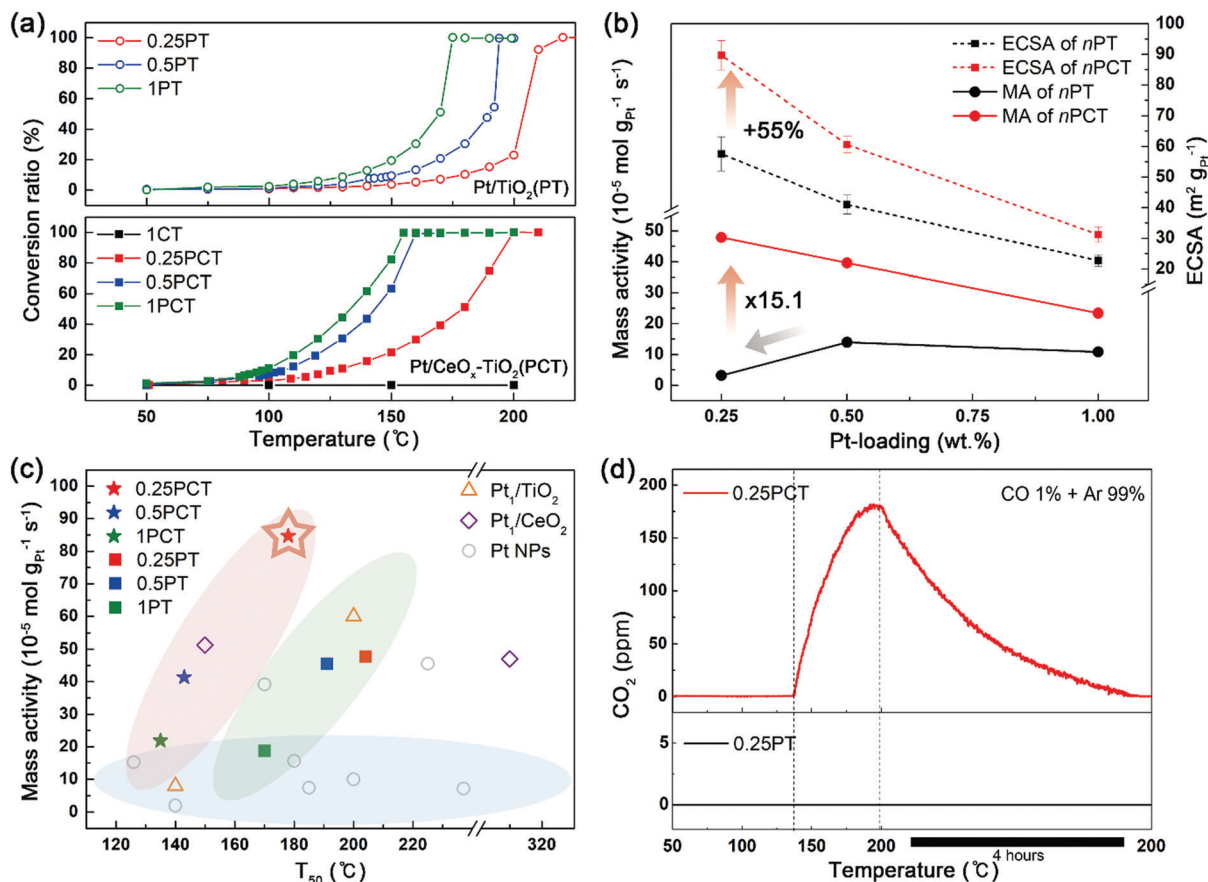


Fig. 5 CO oxidation performance of *n*PT and *n*PCT catalysts. (a) Temperature-programmed CO conversion profile (light-off curve) of the *n*PT and *n*PCT catalysts. (b) The specific mass activity (MA) of the *n*PT and *n*PCT catalysts at 140 °C as a function of Pt-loading and the ECSA of the *n*PT and *n*PCT catalysts. The MA of the *n*PCT catalysts is an inverse function of Pt-loading, whereas the MA of *n*PT is lower than the others. (c) The specific MA values of the *n*PT and *n*PCT catalysts plotted as a function of T_{50} . Reference values were limited to Pt-SAs or NPs supported on conventionally synthesized or purchased CeO_2 or TiO_2 (refer to the ESI† for the full reference list). (d) CO-TPR analysis results of the 0.25PT and 0.25PCT catalysts.

vacancy, thereby completing the overall MvK type reaction pathway. An E_{act} of 0.43 eV was required for dissociation of the Ce-bound O_2 (TS2). Our results show that the CO oxidation pathway involves the lattice oxygen at the tri-phase interface of Pt- CeO_x - TiO_2 oxidizing the first Pt-CO* *via* the MvK mechanism. The relatively higher E_{act} of the first CO oxidation indicates that activation of the lattice oxygen at the Pt₂- CeO_x - TiO_2 interface is the rate-determining step.

The catalytic properties of both *n*PCT and *n*PT were also investigated for CO oxidation in the temperature range of 50–300 °C. Fig. 5a shows the light-off performance of the *n*PT and *n*PCT catalysts, respectively. Clearly, the *n*PCT catalysts oxidize CO more actively than the *n*PT for all Pt-loadings. T_{50} and T_{100} (the temperature of 50% and 100% conversion, respectively) of *n*PT are higher than those of *n*PCT with the same *n* (Table S3 in the ESI†). As shown in Fig. 5b and Table S3 in the ESI†, the specific MA of the *n*PCT samples at 140 °C is always higher than that of *n*PT with the same amount of Pt-loading.

Here, we emphasize that E_{act} of *n*PCT is close to the DFT-calculated E_{act} (0.75 eV) *via* the MvK-type CO oxidation at the Pt₂- CeO_x - TiO_2 interface (Fig. S10 in the ESI†). Therefore, the

MvK type mechanism plays a major role in the *n*PCT catalysts. Despite the relatively higher E_{act} of the *n*PCT catalysts, they exhibited outstanding catalytic performance, higher MA, compared with the *n*PT catalysts with even lower E_{act} . This enhancement can be understood by the presence of Pt-SAs at the CeO_x - TiO_2 interfaces in *n*PCT, as already confirmed by experimental observation (STEM and XAS). It is further supported by an additional CO adsorption measurement, which reveals that the electrochemical surface area (ECSA) in 0.25PCT is 55% higher than that in 0.25PT owing to the preferential formation of Pt-SAs (Fig. 5b).

Notably, despite high ECSA values, the MA of 0.25PT was significantly lower than that of 0.5PT (Fig. 5b and Table S3 in the ESI†). The MA of the *n*PT and *n*PCT catalysts plotted as a function of temperature (Fig. S11 in the ESI†) shows that the MA of 0.25PCT increases upon a temperature increase, assuring the essential role of the MvK mechanism with higher E_{act} . Once the MvK mechanism becomes active above 100 °C, the MA of 0.25PCT rapidly increases at the elevated temperature. In contrast, the MA of 0.25PT does not significantly increase with the temperature increase despite its lower E_{act} . In addition, the MA of 0.25PT is less than that of 0.5PT, which is consistently

observed in the whole temperature range. These findings are indicative of CO poisoning of the Pt species in 0.25PT.

Our DFT calculation results confirm that the Pt-SAs formed at the $\text{CeO}_x\text{-TiO}_2$ interface are immune to surface poisoning by CO and thus activate the MvK type CO oxidation (Fig. S12 in the ESI†). In contrast to 0.25PCT, the high CO_2 production energy of 1.28 eV calculated from the CO-saturated $\text{TiO}_2(101)$ supported Pt₉ NP, which represents small Pt NPs in 0.25PT, predicts that the MvK type CO oxidation pathway is energetically forbidden in 0.25PT (Fig. S12 in the ESI†). As a result, our 0.25PCT exhibits the best MA– T_{50} balance among the previously reported TiO_2 or CeO_2 supported Pt-SA and NP catalysts (Fig. 5c). Moreover, our 0.25PCT catalyst was synthesized by a simple and hierarchical chemical route. The consistent light-off performance of the 0.25PCT catalyst for six repeated CO oxidation cycles suggests that the catalytic nature of the Pt-SAs at the $\text{CeO}_x\text{-TiO}_2$ interfaces is well-preserved during long-term operation (Fig. S13 in the ESI†). This result convinces us that stabilizing potential based interface design is successful to improve the MA as well as stability of Pt-SAs. The long-term temperature- and time-resolved stability test results of Pt-SAs supported on TiO_2 and $\text{CeO}_x\text{-TiO}_2$ will be studied in future work.

To directly unravel the operation of the MvK mechanism in the *n*PCT catalysts, we performed complementary CO-temperature programmed reduction (TPR) analysis with the 0.25PT and 0.25PCT catalysts (Fig. 5d). The CO-TPR analysis was performed under a stream of 1% of CO balanced with 99% of Ar without any

oxygen supply, therefore the oxygen to participate in the CO oxidation should be supplied through the Pt– $\text{CeO}_x\text{-TiO}_2$ or the Pt– TiO_2 interfaces. Fig. 5d shows that CO_2 was produced in 0.25PCT at above 135 °C whereas no CO_2 was detected in 0.25PT. This result provides convincing evidence about the presence of the CO-tolerant Pt-SAs and the CO-poisoned Pt species in 0.25PCT and 0.25PT, respectively.

Synchrotron-based *operando* gas STXM was utilized to validate the operation of the MvK mechanism (Fig. 6a). The MvK mechanism can be completely identified by probing XAS across the Ce M-edge under the same condition as CO-TPR. The results presented in Fig. 6b and c reveal that the production of CO_2 in 0.25PCT accompanies the reduction of Ce^{4+} to Ce^{3+} , which results from the loss of oxygen at the Pt– $\text{CeO}_x\text{-TiO}_2$ interfaces as shown schematically in Fig. 6a. The reaction temperature at which the $\text{Ce}^{4+}/\text{Ce}^{3+}$ ratio is significant is consistent with that of CO_2 production from CO-TPR. Our CO-TPR and *operando* XAS results strongly indicate the presence of the CO-tolerant Pt-SAs in the 0.25PCT catalyst and the operation of the interface-mediated MvK mechanism of CO oxidation.

Conclusions

We present the catalytic supremacy of dense Pt-SAs achieved by tailoring the chemical nature of the multi-component interface with atomic precision. Addition of 1 wt% Ce to TiO_2 supporting oxide powders creates $\text{CeO}_x\text{-TiO}_2$ interfaces that physically disintegrate Pt into Pt-SAs and activate the interface-mediated MvK mechanism of CO oxidation, while preserving its catalytic activity against CO-poisoning. As a result, the Pt-SAs stabilized at the $\text{CeO}_x\text{-TiO}_2$ hybrid interfaces increase the MA of Pt toward CO oxidation by 15.1 times at 140 °C, showing the highest mass activity among similar systems reported so far. We adopt synchrotron-based *operando* liquid/gas scanning transmission X-ray microscopy (STXM) to probe the spatio-temporal evolution of the Ce oxidation state, which indicates the preferred growth of Pt-SAs at the $\text{CeO}_x\text{-TiO}_2$ interfaces and the interface-mediated reaction mechanism in CO oxidation for the first time. Our comprehensive study of DFT calculations, *operando* STXM analyses, and experimental catalyst performance test results presents a novel design strategy of Pt-SA catalysts by atomically precise interface engineering toward efficient use of Pt catalysts.

Conflicts of interest

There are no conflicts to declare.

Acknowledgements

This work was supported by a National Research Foundation of Korea (NRF) grant funded by the Korea government (MSIP) (NRF-2017R1A2B4009829 and NRF-2019R1A2C1089256). H. Y. K. is thankful for the support from the KIST Institutional Program

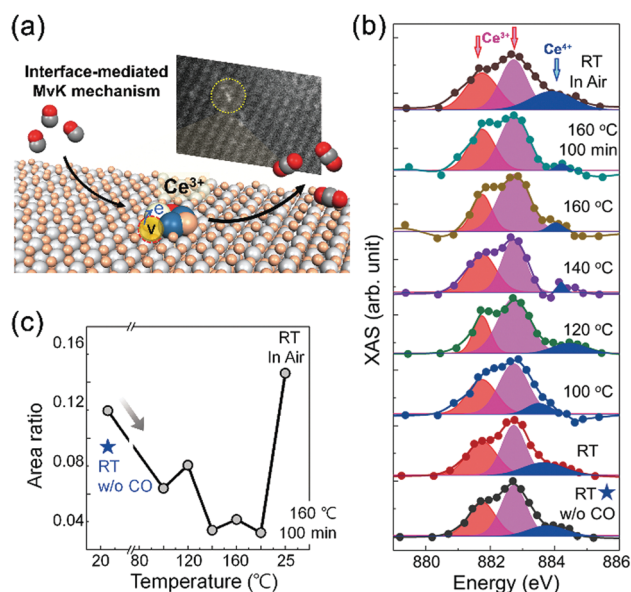


Fig. 6 *Operando* gas phase XAS analysis. (a) Schematic diagram of Ce reduction upon CO oxidation by the MvK mechanism at the Pt– $\text{CeO}_x\text{-TiO}_2$ interface. (b) *Operando* XAS with respect to reaction temperatures. Owing to the low signal-to-noise ratio, XAS was obtained from the entire particle region. De-convoluted spectral features for Ce^{3+} (red and magenta shaded areas, energy positions are indicated by the red arrows) and Ce^{4+} (blue shaded area, energy positions are indicated by the blue arrow) are superimposed on the averaged XAS. (c) Area ratio between the de-convoluted spectral features of Ce^{3+} and Ce^{4+} in (b).

(2E29280-19-108). S. L. and W. J. are thankful for the support from a National Research Foundation of Korea (NRF) grant funded by the Korea government (MSIP) (NRF-2017M3A7B4049547, NRF-2019R1A2C2006006, and NRF-2019M3E6A1064523). C. K. is thankful for the support from the Creative Materials Discovery Program through the National Research Foundation of Korea (NRF) funded by the Ministry of Science, ICT and Future Planning (NRF-2017M3D1A1039561). This research used resources of the Center for Functional Nanomaterials, which is a U.S. DOE Office of Science Facility, and the Scientific Data and Computing Center, a component of the Computational Science Initiative, at Brookhaven National Laboratory under Contract No. DE-SC0012704. Computing time was also provided by the National Institute of Supercomputing and Network/Korea Institute of Science and Technology Information (KSC-2018-CRE-0078). The work of Y.-S. Y., R. C., M. A. M., K. N., D. T., and D. A. S. was supported by the Director, Office of Science, Office of Basic Energy Sciences, of the US Department of Energy (Contract no. DE-AC02-05CH11231). This research used resources of the Advanced Light Source, which is a DOE Office of Science User Facility under contract no. DEAC02-05CH11231.

Notes and references

- 1 E. W. McFarland and H. Metiu, *Chem. Rev.*, 2013, **113**, 4391–4427.
- 2 Q. Fu, H. Saltsburg and M. Flytzani-Stephanopoulos, *Science*, 2003, **301**, 935–938.
- 3 S. Vajda, M. J. Pellin, J. P. Greeley, C. L. Marshall, L. A. Curtiss, G. A. Ballentine, J. W. Elam, S. Catillon-Mucherie, P. C. Redfern, F. Mehmood and P. Zapol, *Nat. Mater.*, 2009, **8**, 213–216.
- 4 E. C. Tyo and S. Vajda, *Nat. Nanotechnol.*, 2015, **10**, 577–588.
- 5 A. A. Herzing, C. J. Kiely, A. F. Carley, P. Landon and G. J. Hutchings, *Science*, 2008, **321**, 1331–1335.
- 6 J. Jones, H. Xiong, A. T. DeLaRiva, E. J. Peterson, H. Pham, S. R. Challa, G. Qi, S. Oh, M. H. Wiebenga, X. I. Pereira Hernández, Y. Wang and A. K. Datye, *Science*, 2016, **353**, 150–154.
- 7 L. Nie, D. Mei, H. Xiong, B. Peng, Z. Ren, X. I. P. Hernandez, A. DeLaRiva, M. Wang, M. H. Engelhard, L. Kovarik, A. K. Datye and Y. Wang, *Science*, 2017, **358**, 1419–1423.
- 8 X.-F. Yang, A. Wang, B. Qiao, J. Li, J. Liu and T. Zhang, *Acc. Chem. Res.*, 2013, **46**, 1740–1748.
- 9 B. Qiao, A. Wang, X. Yang, L. F. Allard, Z. Jiang, Y. Cui, J. Liu, J. Li and T. Zhang, *Nat. Chem.*, 2011, **3**, 634–641.
- 10 S. Wei, A. Li, J. C. Liu, Z. Li, W. Chen, Y. Gong, Q. Zhang, W. C. Cheong, Y. Wang, L. Zheng, H. Xiao, C. Chen, D. Wang, Q. Peng, L. Gu, X. Han, J. Li and Y. Li, *Nat. Nanotechnol.*, 2018, **13**, 856–861.
- 11 A. Wang, J. Li and T. Zhang, *Nat. Rev. Chem.*, 2018, **2**, 65–81.
- 12 L. Zhang, K. Doyle-Davis and X. Sun, *Energy Environ. Sci.*, 2019, **12**, 492–517.
- 13 X. Zhang, H. Shi and B.-Q. Xu, *Angew. Chem., Int. Ed.*, 2005, **44**, 7132–7135.
- 14 J. Shan, M. Li, L. F. Allard, S. Lee and M. Flytzani-Stephanopoulos, *Nature*, 2017, **551**, 605.
- 15 X. Cui, K. Junge, X. Dai, C. Kreyenschulte, M.-M. Pohl, S. Wohlrab, F. Shi, A. Brückner and M. Beller, *ACS Cent. Sci.*, 2017, **3**, 580–585.
- 16 A. Beniya and S. Higashi, *Nat. Catal.*, 2019, **2**, 590–602.
- 17 R. Lang, W. Xi, J.-C. Liu, Y.-T. Cui, T. Li, A. F. Lee, F. Chen, Y. Chen, L. Li, L. Li, J. Lin, S. Miao, X. Liu, A.-Q. Wang, X. Wang, J. Luo, B. Qiao, J. Li and T. Zhang, *Nat. Commun.*, 2019, **10**, 234.
- 18 Y.-Q. Su, Y. Wang, J.-X. Liu, I. A. W. Filot, K. Alexopoulos, L. Zhang, V. Muravev, B. Zijlstra, D. G. Vlachos and E. J. M. Hensen, *ACS Catal.*, 2019, **9**, 3289–3297.
- 19 J.-C. Liu, Y.-G. Wang and J. Li, *J. Am. Chem. Soc.*, 2017, **139**, 6190–6199.
- 20 Y. G. Wang, D. Mei, V. A. Glezakou, J. Li and R. Rousseau, *Nat. Commun.*, 2015, **6**, 6511.
- 21 Y. Nagai, T. Hirabayashi, K. Dohmae, N. Takagi, T. Minami, H. Shinjoh and S. i. Matsumoto, *J. Catal.*, 2006, **242**, 103–109.
- 22 Y. Choi, S. K. Cha, H. Ha, S. Lee, H. K. Seo, J. Y. Lee, H. Y. Kim, S. O. Kim and W. Jung, *Nat. Nanotechnol.*, 2019, **14**, 245–251.
- 23 M. Cargnello, V. V. T. Doan-Nguyen, T. R. Gordon, R. E. Diaz, E. A. Stach, R. J. Gorte, P. Fornasiero and C. B. Murray, *Science*, 2013, **341**, 771–773.
- 24 H. Ha, S. Yoon, K. An and H. Y. Kim, *ACS Catal.*, 2018, **8**, 11491–11501.
- 25 K. Ding, A. Gulec, A. M. Johnson, N. M. Schweitzer, G. D. Stucky, L. D. Marks and P. C. Stair, *Science*, 2015, **350**, 189–192.
- 26 L. DeRita, S. Dai, K. Lopez-Zepeda, N. Pham, G. W. Graham, X. Pan and P. Christopher, *J. Am. Chem. Soc.*, 2017, **139**, 14150–14165.
- 27 P. Mars and D. W. van Krevelen, *Chem. Eng. Sci.*, 1954, **3**, 41–59.
- 28 H.-J. Freund, G. Meijer, M. Scheffler, R. Schlögl and M. Wolf, *Angew. Chem., Int. Ed.*, 2011, **50**, 10064–10094.
- 29 M. Zammit, C. DiMaggio, C. Kim, C. Lambert, G. Muntean, C. Peden, J. Parks and K. Howden, *Future Automotive After-treatment Solutions: The 150 °C Challenge Workshop Report*, 2013.
- 30 T. Barakat, J. C. Rooke, E. Genty, R. Cousin, S. Siffert and B.-L. Su, *Energy Environ. Sci.*, 2013, **6**, 371–391.
- 31 H. Y. Kim and P. Liu, *ChemCatChem*, 2013, **5**, 3673–3679.
- 32 R. A. Lemons, *J. Power Sources*, 1990, **29**, 251–264.
- 33 K. Liu, A. Wang and T. Zhang, *ACS Catal.*, 2012, **2**, 1165–1178.
- 34 J. Saavedra, T. Whittaker, Z. Chen, C. J. Pursell, R. M. Rioux and B. D. Chandler, *Nat. Chem.*, 2016, **8**, 584.
- 35 D. Widmann, E. Hocking and R. J. Behm, *J. Catal.*, 2014, **317**, 272–276.
- 36 S. Alayoglu, A. U. Nilekar, M. Mavrikakis and B. Eichhorn, *Nat. Mater.*, 2008, **7**, 333–338.
- 37 L. Cao, W. Liu, Q. Luo, R. Yin, B. Wang, J. Weissenrieder, M. Soldemo, H. Yan, Y. Lin, Z. Sun, C. Ma, W. Zhang, S. Chen, H. Wang, Q. Guan, T. Yao, S. Wei, J. Yang and J. Lu, *Nature*, 2019, **565**, 631–635.

- 38 X. I. Pereira-Hernández, A. DeLaRiva, V. Muravev, D. Kunwar, H. Xiong, B. Sudduth, M. Engelhard, L. Kovarik, E. J. M. Hensen, Y. Wang and A. K. Datye, *Nat. Commun.*, 2019, **10**, 1358.
- 39 A. M. Gänzler, M. Casapu, P. Vernoux, S. Loridant, F. J. Cadete Santos Aires, T. Epicier, B. Betz, R. Hoyer and J.-D. Grunwaldt, *Angew. Chem., Int. Ed.*, 2017, **56**, 13078–13082.
- 40 L. A. J. Garvie and P. R. Buseck, *J. Phys. Chem. Solids*, 1999, **60**, 1943–1947.
- 41 H. Y. Kim, M. S. Hybertsen and P. Liu, *Nano Lett.*, 2017, **17**, 348–354.
- 42 A. C. Johnston-Peck, S. D. Senanayake, J. J. Plata, S. Kundu, W. Xu, L. Barrio, J. Graciani, J. F. Sanz, R. M. Navarro, J. L. G. Fierro, E. A. Stach and J. A. Rodriguez, *J. Phys. Chem. C*, 2013, **117**, 14463–14471.
- 43 S. Luo, T.-D. Nguyen-Phan, A. C. Johnston-Peck, L. Barrio, S. Sallis, D. A. Arena, S. Kundu, W. Xu, L. F. J. Piper, E. A. Stach, D. E. Polyansky, E. Fujita, J. A. Rodriguez and S. D. Senanayake, *J. Phys. Chem. C*, 2015, **119**, 2669–2679.
- 44 F. Dvořák, M. Farnesi Camellone, A. Tovt, N.-D. Tran, F. R. Negreiros, M. Vorokhta, T. Skála, I. Matolínová, J. Mysliveček, V. Matolín and S. Fabris, *Nat. Commun.*, 2016, **7**, 10801.